

Reflection-Based Relative Localization for Cooperative UAV Teams Using Active Markers

Tim Lakemann¹, Daniel Bonilla Licea^{1,2}, Viktor Walter¹ and Martin Saska¹

Abstract—Reflections of active markers in the environment are a common source of ambiguity in onboard visual relative localization. This work presents a novel approach for onboard relative localization in multi-robot teams that exploits these typically unwanted reflections of active markers in the environment. It operates without prior knowledge of robot size or predefined marker configurations and remains independent of surface properties, an essential feature for heterogeneous micro-aerial swarms cooperating in unknown environments. It explicitly accounts for uncertainties caused by non-flat surfaces, with a particular focus on dynamic water surfaces, which are especially relevant for marine deployments. We validated the approach in both indoor and outdoor experiments, demonstrating that the proposed reflection-based localization system operates reliably without prior knowledge of team member size and achieves greater effective range (above 30 m) and accuracy than state-of-the-art methods. The video and source code of this work will be made publicly available after publication.

Index Terms—Aerial Systems; Perception and Autonomy, Localization, Multi-Robot Systems

I. INTRODUCTION

Reliable relative localization among team members is crucial for multi-robot systems to collaboratively execute tasks safely and reliably [1]. In outdoor environments, Global Navigation Satellite System (GNSS) often lacks the reliability needed for close-formation flight. Its signal accuracy and precision are particularly degraded in dense forests, natural landscapes, or urban canyons, and in some cases, it becomes entirely unavailable [2], [3], [4]. While Real-Time Kinematic (RTK) antennas enhance reliability, they also limit the operational space of the Uncrewed Aerial Vehicles (UAVs) [4].

In indoor settings, Motion capture (MoCap) systems are commonly used for relative localization [5]. However, the coverage area of the MoCap system limits the movement of the UAV [6]. This limitation makes them unsuitable for exploration tasks in unknown environments. Additionally, all aforementioned techniques rely on stable communication links, which can be a limiting factor in many practical scenarios.

Onboard relative localization eliminates the dependence on external infrastructure, expands operational flexibility, and allows deployment without communication between team members. Vision-based methods provide a cost-effective, compact, and lightweight solution for large-scale multi-robot

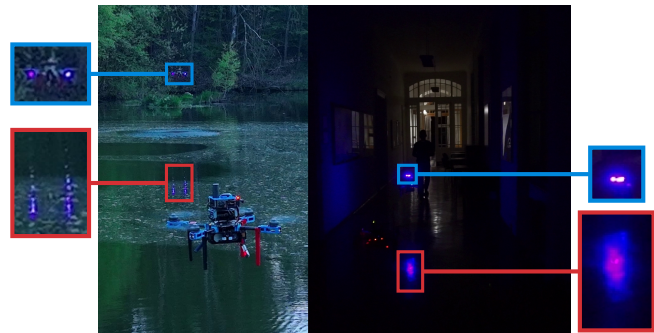


Fig. 1: Outdoor (left) and indoor dark (right) experiments: A UAV estimates the relative position by using surface reflections from active markers attached to a team member UAV. Blue boxes: the UAV with active markers attached. Red box: Surface reflections of the light emitted by the UAV.

systems [7], [8], [9]. While passive markers like AprilTags improve localization accuracy, they impose constraints on system dynamics, which is particularly critical for UAVs [6], [10]. Unlike passive markers, active markers attached to UAVs overcome limitations related to marker size and enable reliable detection under varying lighting conditions [11], [12]. Most relative localization and pose estimation systems require prior knowledge of the active marker configuration on the UAVs to accurately estimate the relative distance, which is determined based on the pixel distance between markers in the image [9], [12], [13].

However, as with marker-less or passive marker systems, the precision of distance estimation decreases for micro-aerial vehicles with closely spaced markers. On micro UAVs, markers often appear too close together or merge into a single pixel at certain distances, especially when using low-resolution cameras. As a result, distance estimation accuracy is limited for micro-scale platforms.

This work addresses these limitations by introducing a novel relative localization system for multi-robot teams that uses surface reflections – typically considered undesirable and a source of ambiguity in localization systems. The proposed method is motivated by mission scenarios with reflective surfaces, such as maritime environmental monitoring and nighttime outdoor surveillance, as well as indoor tasks like subterranean navigation and warehouse inventory, where polished floors often create reflections (Fig. 1). Our approach is also motivated by the need for collaborative multi-robot systems operating in challenging non-line-of-sight scenarios.

Previous works have focused on mitigating these reflec-

¹Multi-Robot Systems Group, Faculty of Electrical Engineering, Czech Technical University in Prague, Technicka 2, Prague, Czech Republic, lakentim|waltevik|martin.saska@fel.cvut.cz

² Mohammed VI Polytechnic University, Morocco daniel.bonilla@um6p.ma

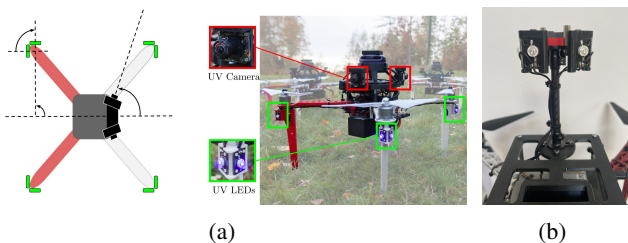


Fig. 2: (a) UVDAR system estimating relative position using the known spacing between UV-LEDs attached to a UAV [23]. (b) UV-LED array attached to a UAV, used in our indoor experiment for relative localization.

tions: [14], [15] used polarization filters to suppress surface reflections, while [16] combined structured light with polarization filters for improved depth estimation. Several studies have explored reflection-based localization using the radio frequency (RF) spectrum [17], [18], [19]. Additional research has investigated sound-source localization in non-line-of-sight scenarios [20], [21]. In [22], depth images of static scenes were generated from reflections on specular water surfaces using a stationary camera. However, this approach is limited to mirror-like water surfaces and requires 40 seconds per 400×500 -pixel image, making it impractical for collaborative UAVs operating in dynamic environments with limited onboard resources and irregular or non-smooth surface structures.

To the best of our knowledge, relative localization through surface reflections for multi-robot systems remains unexplored in literature. Unlike most vision-based relative localization methods, our approach takes advantage of surface reflections to extend the operational range while remaining unaffected by surface properties (e.g., specular reflections) or the size of the UAV and geometry. By accounting for the spread in the reflection pattern caused by surface irregularities (Fig. 3) and sensor uncertainties, the proposed approach improves reliability. Since the marker and its reflection appear much farther apart in the image than their actual spacing on the UAV, the method improves the accuracy and precision of position estimation. Additionally, its independence from marker geometry allows for the use of more compact markers, enabling flexible attachment to micro-UAV.

We evaluated the proposed approach in diverse indoor and outdoor environments, demonstrating its ability to accurately estimate the relative position between two UAVs, outperforming state-of-the-art methods. This enables an efficient solution for close cooperative formation flights in confined indoor environments and marine operations. Our contribution in this work is threefold:

- 1) We derive the theoretical background with the underlying physics for reflection-based localization.
- 2) We propose a novel camera-only reflection-based relative localization approach that requires no prior knowledge of team member sizes or surface properties.

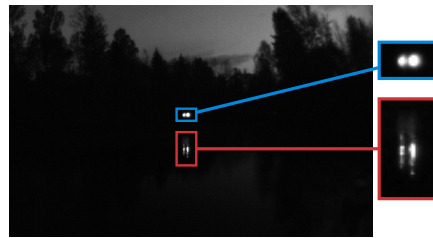


Fig. 3: Excerpt from an outdoor experiment showing active markers attached to the UAV (blue) and their diffuse reflections on the water surface (red), captured onboard the UAV.

- 3) We experimentally verified that the proposed approach significantly enhances the operational potential of micro-scale teams in both indoor and outdoor environments, regardless of lighting conditions. Significant performance improvements are also demonstrated in comparison to state-of-the-art methods.

II. THEORETICAL BACKGROUND

In this section, we provide a theoretical overview of the interaction between unpolarized light, such as that emitted by most Light-emitting diodes (LEDs), and the surface properties that influence the reflected energy captured by the camera of the observer. We model the light emitted by the LEDs of the UAVs as an unpolarized electromagnetic plane wave. When this wave transitions from one medium to another, the law of refraction and the Fresnel equations describe the distribution of energy between the reflected and transmitted waves. As stated in [24], assuming that the permeabilities of both media are approximately equal to that of free space, μ_0 , the reflected power of an unpolarized wave, commonly referred to as the reflection power coefficient, is given by the average of the reflection coefficients for perpendicular and parallel polarizations:

$$P_r = \frac{1}{2} \left(\frac{n_t \cos \theta_i - n_i \cos \theta_t}{n_i \cos \theta_t + n_t \cos \theta_i} + \frac{n_i \cos \theta_i - n_t \cos \theta_t}{n_i \cos \theta_i + n_t \cos \theta_t} \right). \quad (1)$$

The refractive indices of the two media are denoted by n_i (incident medium) and n_t (transmitting medium), and the angles of incidence and transmission are denoted by θ_i and θ_t , respectively. As the angle of incidence θ_i increases, the reflected light intensity increases correspondingly.

In addition to the incident angle and refractive indices, the visibility of the reflection at the observer depends on the surface smoothness. A surface is considered smooth if its irregularities are small relative to the wavelength of the electromagnetic wave, leading to specular reflection (Fig. 4) [25]. For still water or shiny floors and walls, specular reflections are expected, while rough water or textured indoor surfaces tend to produce diffuse reflections. Most human-made surfaces in office-like and industrial environments fall between these extremes [25]. Moreover, the light emitted by the transmitting UAV spreads across the reflective surface, appearing vertically elongated on the floor and horizontally

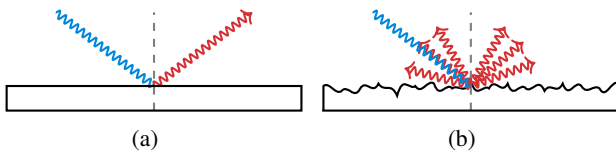


Fig. 4: Two extreme cases: Incident light (blue) undergoes (a) specular and (b) diffuse reflection (red).

elongated on the walls in the image captured by the observer (Fig. 1 and Fig. 3). If the light source does not exhibit a spherical radiation pattern, the orientation of the UAV influences the effective power reaching the surface boundary. For a UAV equipped with Lambertian radiators that emit their maximum power in the forward direction, higher speeds result in a greater roll and pitch angle, which directs more energy from the LED towards the vertical surface and increases the reflected energy observed by the receiver. The reflected light captured by the camera of the observer is primarily influenced by the surface properties of the material. For instance, the roughness of a floor is often modeled using a Gaussian height distribution [26], while water surfaces typically exhibit dynamic, time-varying waves. Outdoor water surfaces are particularly subject to disturbances such as wind, which disrupts what would otherwise be specular reflections. When multiple UAVs fly over the water, additional disturbances are introduced by the airflow generated by their propellers, see Figs. 1 and 8. These disturbances can be approximated using capillary-gravity wave models, which describe surface waves influenced by surface tension for wavelengths below 1 cm and gravity for longer wavelengths [27]. The motions of the UAVs over the water surface influence the amplitude and wavelength of the capillary-gravity waves. Additional wind effects introduce unpredictable fluctuations, which would significantly complicate the position estimation system by incorporating surface properties. Therefore, in the next section, we derive a model that is independent of both the motion of the UAVs and the surface properties.

III. REFLECTION-BASED LOCALIZATION METHOD

The proposed reflection-based relative localization method works effectively both indoors and outdoors, regardless of UAV size or surface properties. Although the proposed system currently uses only ground reflections, it can be extended to wall reflections if the wall distance is known, for instance, from a Light Detection And Ranging (LIDAR) sensor. First, we apply static binarization to the image, followed by Connected Component Analysis (CCA) to extract centroids. These centroids are then classified into three categories: direct UAV-emitted light, its surface reflections, and background elements like a bright sky. Centroids associated with a UAV are identified based on their emitted signal [23]. Reflection centroids are identified as those positioned vertically below a direct UAV-emitted light centroid, while background centroids are selected based on their consistent presence and size in the image. For simplicity, we derive in

the following the reflection-based position estimation for a single UAV.

Let p_d denote the centroid pixel corresponding to the direct UAV-emitted light and p_r the centroid of its reflection. For a calibrated fisheye camera, the pixel coordinates of p_d and p_r can be converted into 3D unit bearing vectors using the function *cam2world*, which is available in various computer vision libraries, such as *OCamLib* [28]. In the following, the coordinate origin is defined at the body frame of the observer. The x -axis aligns with the horizontal center of the camera and is parallel to the surface, the y -axis is also parallel to the surface, and the z -axis points upwards (Fig. 5a). To account for the roll (ψ) and pitch (ϕ) angles of the observing aircraft, the 3D unit bearing vectors corresponding to p_d and p_r are transformed as follows:

$$\vec{b}_d = [\hat{x}_d, \hat{y}_d, \hat{z}_d]^\top = \mathbf{R}(-\psi)\mathbf{R}(-\phi)\text{cam2world}(p_d), \quad (2)$$

$$\vec{b}_r = [\hat{x}_r, \hat{y}_r, \hat{z}_r]^\top = \mathbf{R}(-\psi)\mathbf{R}(-\phi)\text{cam2world}(p_r), \quad (3)$$

where $\mathbf{R}(-\psi)$ and $\mathbf{R}(-\phi)$ are the rotation matrices that compensate for the roll and pitch of the observing UAV, respectively.

As shown in Fig. 5, the center of the reflection, denoted by \vec{r} , is retrieved using the two angles β_r and θ_r , which are defined as follows:

$$\beta_r = \arctan \frac{|\hat{z}_r|}{\hat{x}_r}, \quad (4)$$

$$\theta_r = \arctan \frac{\hat{y}_r}{\hat{x}_r}. \quad (5)$$

Thus, the center of the reflection, \vec{r} , is determined using equations (3) to (5), along with the height of the observer, z_o :

$$\begin{aligned} \vec{r} &= [r_x \ r_y \ r_z]^\top \\ &= \left[|z_o| \frac{\hat{x}_r}{|\hat{z}_r|} \quad |z_o| \frac{\hat{y}_r}{|\hat{z}_r|} \quad -z_o \right]^\top. \end{aligned} \quad (6)$$

As illustrated in Fig. 1 and 3, the light emitted by the UAV and its reflection on a surface appears elongated along the viewing axis. Two factors cause this elongation: the geometric projection of the reflected light at shallow incidence angles and the scattering induced by surface roughness. To represent the spread in the reflection, we construct an ellipse centered at p_r . The minor and major axes are defined by the farthest pixels from p_r in the vertical (p_v) and horizontal (p_h) directions, respectively. These pixels are selected based on their intensity exceeding a predefined threshold σ within a local bounding box around p_r . To retrieve the vectors representing the minor and major axis of the ellipse, equations (3) to (5) can be applied to p_v and p_h yielding:

$$\vec{r}_v = \left[|z_o| \frac{\hat{x}_v}{|\hat{z}_v|} \quad |z_o| \frac{\hat{y}_v}{|\hat{z}_v|} \quad -z_o \right]^\top. \quad (7)$$

$$\vec{r}_h = \left[|z_o| \frac{\hat{x}_h}{|\hat{z}_h|} \quad |z_o| \frac{\hat{y}_h}{|\hat{z}_h|} \quad -z_o \right]^\top. \quad (8)$$

Using equations (6) to (8), we construct an elliptical cone (red in Fig. 5a). The apex of the cone is defined by the vector:

$$\vec{a} = [0 \ 0 \ -2z_o]^\top. \quad (9)$$

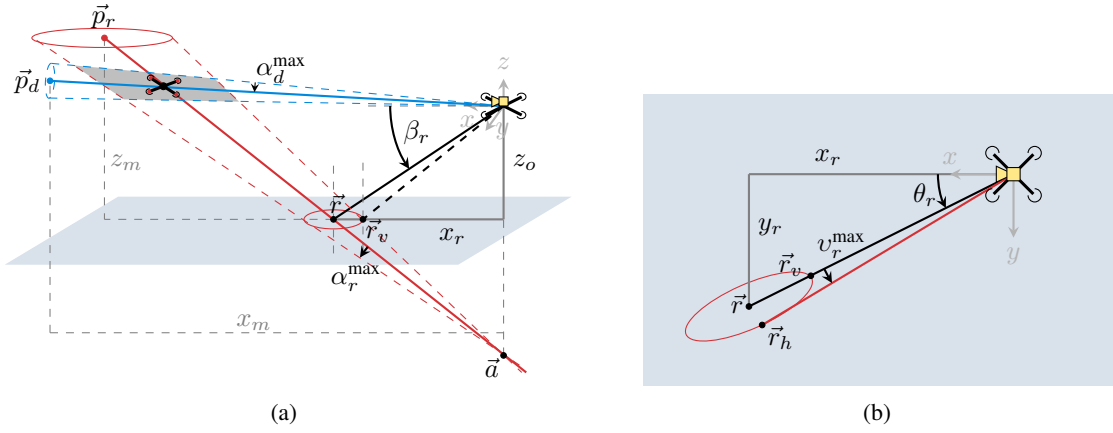


Fig. 5: One UAV equipped with a camera (yellow) constructs an elliptical cone based on the diffuse reflections of light emitted by the transmitting UAV (top left). (a) Side view of our approach, showing the potential location of the transmitting UAV determined by the intersection of two elliptical cones (gray area). (b) Top-down view of the observer UAV with the ellipse around the diffuse reflection.

The half-apex angle of the cone along the vertical axis is given by:

$$\alpha_r^{\max} = \beta_v - \beta_r, \quad (10)$$

which corresponds to the major axis of the ellipse defined by the distance between \vec{r} and \vec{r}_v (Fig. 5a). As shown in Fig. 5b, the horizontal spread of the cone along the horizontal axis (corresponding to the minor axis of the ellipse) defines the half-apex angle:

$$v_r^{\max} = \arctan \frac{\|\vec{r}_h - \vec{r}\|_{xy}}{\|\vec{r} - \vec{a}\|_{xy}}, \quad (11)$$

in the x - y plane. Using a predefined maximum height (z_m), we define the end point of the elliptical cone by the vector:

$$\vec{p}_r = \begin{bmatrix} r_x + z_m \frac{\hat{x}_r}{|\hat{z}_r|} \\ r_y + z_m \frac{\hat{y}_r}{|\hat{z}_r|} \\ z_m \end{bmatrix}. \quad (12)$$

With equations (4) to (12), the following parametric equation defines a finite convex elliptical cone:

$$\vec{c}_r(\gamma_r, l_r, \alpha_r, v_r) = \vec{a} + l_r \vec{d}_r + l_r \vec{n}_1 \tan \alpha_r \cos \gamma_r + l_r \vec{n}_2 \tan v_r \sin \gamma_r, \quad (13)$$

where:

$$\begin{aligned} \gamma_r &\in [0, 2\pi], & \alpha_r &\in [0, \alpha_r^{\max}], & v_r &\in [0, v_r^{\max}], \\ l_r &\in [0, \|\vec{p}_r - \vec{a}\|], & \vec{d}_r &= \frac{\vec{p}_r - \vec{a}}{\|\vec{p}_r - \vec{a}\|}, \end{aligned} \quad (14)$$

and \vec{n}_1 is a unit vector perpendicular to \vec{d}_r , while \vec{n}_2 is a unit vector perpendicular to both \vec{d}_r and \vec{n}_1 .

To address uncertainties arising from the limited camera resolution and inaccuracies introduced during binarization and CCA, we define two angles, α_d^{\max} and v_d^{\max} , which represent the vertical and horizontal uncertainties around \vec{b}_d , respectively. These uncertainties are used to create a

finite convex elliptical cone around \vec{b}_d , similar to the cone representation of the reflection vector and its associated uncertainty in (13). This cone is parameterized by:

$$\vec{c}_d(\gamma_d, l_d, \alpha_d, v_d) = l_d \vec{d}_d + l_d \vec{n}_3 \tan \alpha_d \cos \gamma_d + l_d \vec{n}_4 \tan v_d \sin \gamma_d, \quad (15)$$

where:

$$\begin{aligned} \gamma_d &\in [0, 2\pi], & \alpha_d &\in [0, \alpha_d^{\max}], & v_d &\in [0, v_d^{\max}], \\ l_d &\in [0, \|\vec{p}_d\|], & \vec{d}_d &= \frac{\vec{p}_d}{\|\vec{p}_d\|}, \end{aligned} \quad (16)$$

and \vec{n}_3 is perpendicular to \vec{b}_d , and \vec{n}_4 is perpendicular to both \vec{n}_3 and \vec{b}_d . The vector denoting the end point of the apex axis, depends on the predefined maximum extend in the x -direction (x_m) and is expressed as:

$$\vec{p}_d = \begin{bmatrix} x_m & x_m \frac{\hat{y}_d}{\hat{x}_d} & x_m \frac{\hat{z}_d}{\hat{x}_d} \end{bmatrix}^\top \quad (17)$$

The intersection area of the two cones, defined by equations (13) and (15), represents possible locations of the transmitting UAV, resulting in a system of non-linear equations. To estimate the location of the transmitting UAV we employ a random sampling-based approach: we generate a set of vectors $\mathcal{X} = \{\vec{p}_i \sim U\} | i = 1, \dots, n\}$ whose elements verify equation (13), and therefore ensuring they lie within the reflection cone, see Fig. 5. The vectors in \mathcal{X} are generated by sampling the parametric variables from uniform distributions:

$$\begin{aligned} \gamma_r' &\sim U(0, 2\pi), & \alpha_r' &\sim U(0, \alpha_r^{\max}), \\ v_r' &\sim U(0, v_r^{\max}), & l_r' &\sim U(l_{r,min}, \|\vec{p}_r - \vec{a}\|), \end{aligned} \quad (18)$$

where $l_{r,min} = \|\vec{a} - \vec{r}\|$ ensures that only physically feasible points are sampled—i.e., points located above the surface and within the possible intersection volume. To determine whether $\vec{p}_i \in \mathcal{X}$ lies within the cone defined by equation (15)



Fig. 6: Indoor experiments conducted under bright conditions on different floor types (PVC, left; tiles, right) and under dark conditions (center).

and shown in blue in Fig. 5, we first compute its projection onto the cone axis:

$$\vec{p}_{i||} = \text{proj}_{\vec{d}_d} \vec{p}_i = (\vec{p}_i \cdot \vec{d}_d) \vec{d}_d, \quad (19)$$

with \cdot denoting the scalar product, the two inequalities must hold:

$$0 \leq \|\vec{p}_{i||}\| \leq l_d, \quad (20)$$

$$\frac{(\vec{p}_i - \vec{p}_{i||})_y^2}{(\|\vec{p}_{i||}\| \tan v_d^{\max})^2} + \frac{(\vec{p}_i - \vec{p}_{i||})_z^2}{(\|\vec{p}_{i||}\| \tan \alpha_d^{\max})^2} \leq 1. \quad (21)$$

Inequality (20) ensures that the point lies within the extent of the cone along its axis, while inequality (21) ensures that it lies within the cone's elliptical cross-section. If a point in \mathcal{X} satisfies both conditions given by equations (20) and (21), it is included in the inlier set \mathcal{X}_d . The points in \mathcal{X}_d are then used as observations for a particle filter, which propagates particles according to a constant-velocity model and updates their weights using a robust Cauchy kernel. The resulting weighted particle cloud is used to compute the final state estimate of the transmitting UAV.

IV. EXPERIMENTS

We evaluated our system in both indoor and outdoor experiments to assess its performance and accuracy, comparing the results against the current state-of-the-art algorithm. For ground truth, we used Ultra-wideband (UWB) anchors in indoor experiments and RTK in outdoor experiments. The

| Symbol | Indoor | | | | Outdoor | | |
|----------------------------|--------|------|------|------|---------|------|------|
| | 1 | 2 | 3 | 4 | 1 | 2 | 3 |
| n | 1000 | 1000 | 1000 | 1000 | 1000 | 1000 | 1000 |
| α_r^{\max} [°] | 3 | 3 | 3 | 3 | 4 | 4 | 4 |
| α_d^{\max} [°] | 4 | 4 | 4 | 4 | 3 | 3 | 3 |
| v_d^{\max} [°] | 4 | 4 | 4 | 4 | 3 | 3 | 3 |
| x_m [m] | 15 | 15 | 10 | 10 | 40 | 30 | 40 |
| z_m [m] | 2.5 | 2.5 | 2.5 | 2.5 | 10 | 10 | 10 |
| σ | 60 | 60 | 40 | 40 | 40 | 40 | 40 |
| t_{exposure} [ms] | 20 | 20 | 20 | 20 | 3 | 2 | 2.5 |

TABLE I: Parameters for indoor and outdoor experiments.

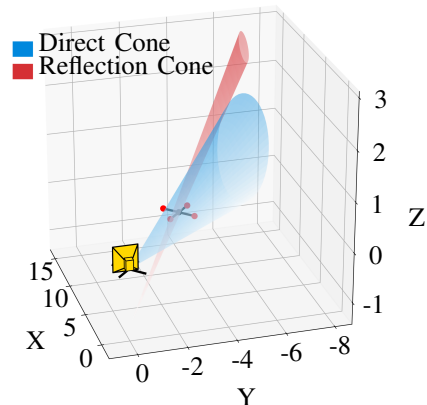


Fig. 7: Elliptical cone towards the light emitted by the transmitting UAV (blue) and elliptical cone constructed based on the reflections on the surface (red), along with the ground truth location of the transmitting UAV.

experiments were conducted using two quadrotor UAVs (one observer and one transmitter) based on the *F450* platform for indoor experiments and the *Holybro X500* platform for outdoor experiments [29]. Each UAV was equipped with an *Intel NUC 10 i7FNK* (6 cores, up to 4.7 GHz). The observer UAV carried a camera with a fisheye lens, Ultraviolet (UV)-bandpass filter, a resolution of 752×480 pixels, and a frame rate of 60 Hz. For outdoor experiments, we mounted UV-LEDs on the arms of the transmitter UAV, with all LEDs emitting an identical signal (Fig. 2a), consistent with the current UltraViolet Direction And Ranging (*UVDAR*) setup [23]. This setup enabled a direct comparison between our reflection-based approach and the *UVDAR* method from [30]. For indoor experiments, we mounted a single circular LED array on top of the UAV, demonstrating the potential applicability of our approach for micro-UAVs (Fig. 2b). Both the proposed method and the *UVDAR* system were executed offline on the same onboard computer (*Intel i7-8550U*, 1.8 GHz) to ensure a fair comparison. Since the observing UAV was hovering, its roll and pitch angles remained below 0.06 rad and were therefore not compensated for. Tab. I summarizes the parameter settings used in the experiments.

A. Indoor

Indoor experiments were conducted under various lighting conditions and on different floor types, including a standard office hallway with a Polyvinyl chloride (PVC) floor

| | 1. PVC (d) | 2. PVC (n) | 3. Tiles (n) | 4. Tiles (n) |
|------------|-----------------|-----------------|-----------------|-----------------|
| MAE(x) [m] | 0.94 ± 0.57 | 1.47 ± 0.40 | 1.28 ± 0.61 | 1.13 ± 0.60 |
| MAE(y) [m] | 0.65 ± 0.54 | 1.13 ± 0.78 | 0.68 ± 0.42 | 0.60 ± 0.42 |
| MAE(z) [m] | 0.20 ± 0.13 | 0.14 ± 0.12 | 0.10 ± 0.09 | 0.10 ± 0.10 |

TABLE II: Mean Absolute Error (MAE) in the x -, y -, and z -axes for indoor experiments conducted under daylight (d) and nighttime (n) conditions on different floor types. Values are reported as mean \pm one standard deviation.



Fig. 8: Outdoor experiment: (Left) Image captured onboard the UAV using a UV-bandpass filter. The centroid of the UAV equipped with active marker system (green) and ellipse (red) of the reflection on the water surface. (Right) Image showing the observing UAV (white), the UAV with the active marker system (green), and its reflections on the surface (red).

| | | X | | | Y | | | Z | | |
|------------|-------|-----------------|-----------------------|------------------|-----------------|------------|------------------|-----------------|------------|-----------------|
| | | MAE[m] | p -value | 95 % CI | MAE[m] | p -value | 95 % CI | MAE[m] | p -value | 95 % CI |
| 1. Outdoor | Ours | 3.50 ± 1.86 | 1.9×10^{-8} | $[-2.62, -1.61]$ | 1.18 ± 0.80 | 0.015 | $[-0.26, -0.07]$ | 1.04 ± 1.57 | 0.917 | $[0.15, 0.42]$ |
| | UVDAR | 5.58 ± 5.77 | | | 1.37 ± 1.09 | | | 0.78 ± 0.83 | | |
| 2. Outdoor | Ours | 2.42 ± 1.50 | 2.0×10^{-5} | $[-0.75, -0.29]$ | 1.73 ± 0.95 | 0.071 | $[-0.16, 0.02]$ | 0.70 ± 0.47 | 0.009 | $[-0.01, 0.07]$ |
| | UVDAR | 2.97 ± 2.14 | | | 1.76 ± 0.97 | | | 0.67 ± 0.44 | | |
| 3. Outdoor | Ours | 5.01 ± 4.15 | 2.2×10^{-11} | $[-1.95, -1.18]$ | 3.29 ± 1.58 | 0.000 | $[-4.89, -4.19]$ | 0.98 ± 0.85 | 0.793 | $[-0.04, 0.11]$ |
| | UVDAR | 7.00 ± 6.03 | | | 7.96 ± 5.60 | | | 0.97 ± 0.67 | | |

TABLE III: Mean Absolute Error (MAE) and one standard deviation along the x -, y -, and z -axes, together with the *Wilcoxon* p -values and 95 % Confidence Interval (CI) of the paired differences, comparing our method with *UVDAR* in outdoor experiments.

and a tiled surface (Fig. 6). The UAVs flew at distances ranging from 2 m to 10 m, while the observing UAV used a downward-facing LIDAR-based rangefinder for height estimation. The *UVDAR* system could not be evaluated in this setup, as the LED array on the transmitting UAV had minimal spacing between LEDs, while the *UVDAR* system requires at least two spatially separated markers. Fig. 7 shows an example of the constructed elliptical cones from the first indoor experiment. Fig. 9 shows the relative position estimates obtained using our approach compared to the ground truth from UWB. Tab. II summarizes the MAEs and corresponding standard deviations for each axis in all experiments. Across all experiments, the estimated distance along the x -axis (optical axis) exhibited the largest MAE.

Despite the limitation that reflections are required for operation, our system reliably tracked the transmitting UAV throughout the flight without prior knowledge of its size or the blob size of the emitted light, relying solely on floor reflections and the known height of the observer.

B. Outdoor

Multiple outdoor experiments with varying exposure time settings were conducted (Tab. I). For example, in the experiment shown in Fig. 3, automatic exposure and gain control were used. We observed that with a maximum exposure time of 3 ms, the camera maintained a stable frame rate (essential for reliable *UVDAR* operation) while reflections remained clearly visible at distances exceeding 20 m on the water surface. The *UVDAR* system provides uncertainty

estimates to account for potential ambiguities in position, but we excluded these from our evaluation, as their spread is typically large and less informative for our analysis.

Fig. 10 shows the three most relevant outdoor flights, comparing the relative positions obtained from our method, *UVDAR*, and the ground truth. Our reflection-based approach maintained high accuracy at distances beyond 30 m, whereas *UVDAR* struggled to provide reliable estimates past 20 m. This highlights the advantage of our approach, which operates without prior knowledge of the UAV size or the configuration of its light sources.

Tab. III summarizes the MAEs and standard deviations for each axis across all experiments, along with the *Wilcoxon* p -values and 95 % CI of the paired differences. Along the z -axis, *UVDAR* achieved slightly lower MAE values (by 1–25 %), but the differences were not statistically significant (p -value ≥ 0.05). Along the y -axis, our method reduced the MAE by 13.9 % and 58.7 % in experiments 1 and 3 (p -value < 0.05 , 95 % CI fully below zero), whereas no statistically significant difference was observed in experiment 2. Along the x -axis (optical axis), our method reduced the MAE by 18.5–37.3 % compared to *UVDAR*, with the difference being statistically significant (p -value < 0.05 , 95 % CI fully below zero).

Overall, our method yielded higher precision in position estimates than *UVDAR*, particularly along the x - and y -axes and at distances exceeding 30 m.

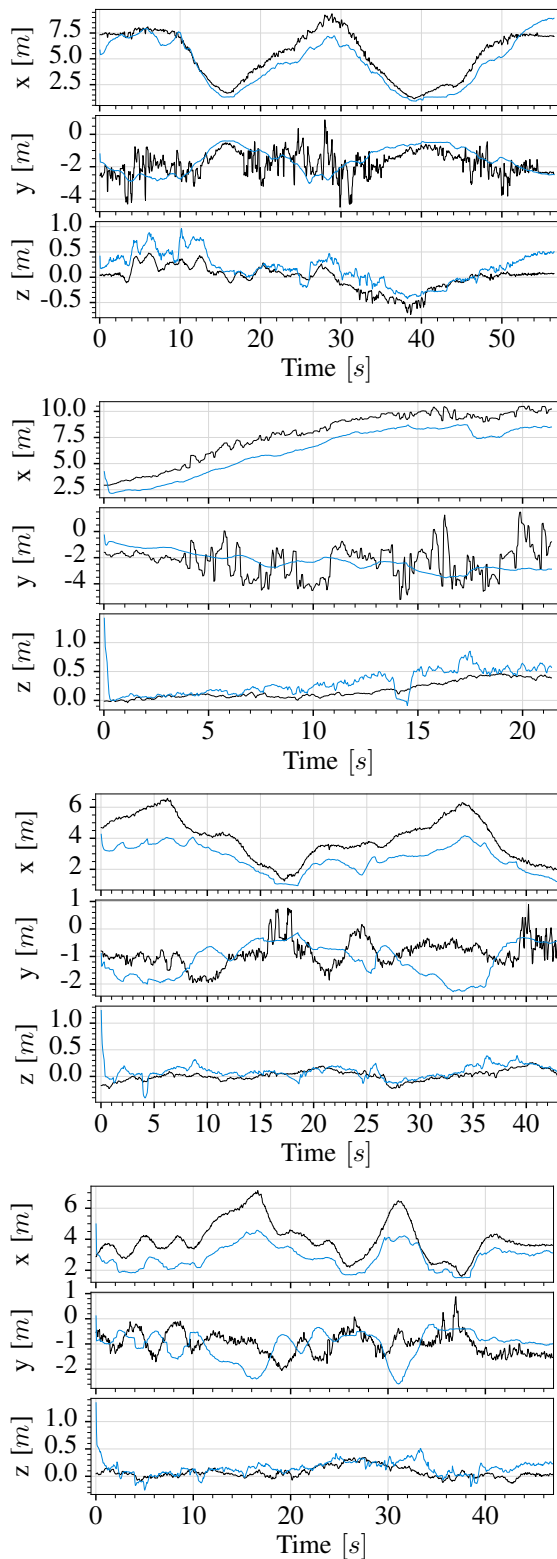


Fig. 9: Relative position estimates obtained using our approach (blue) compared to the relative position ground truth from UWB (black) during indoor experiments 1–4 (from top to bottom).

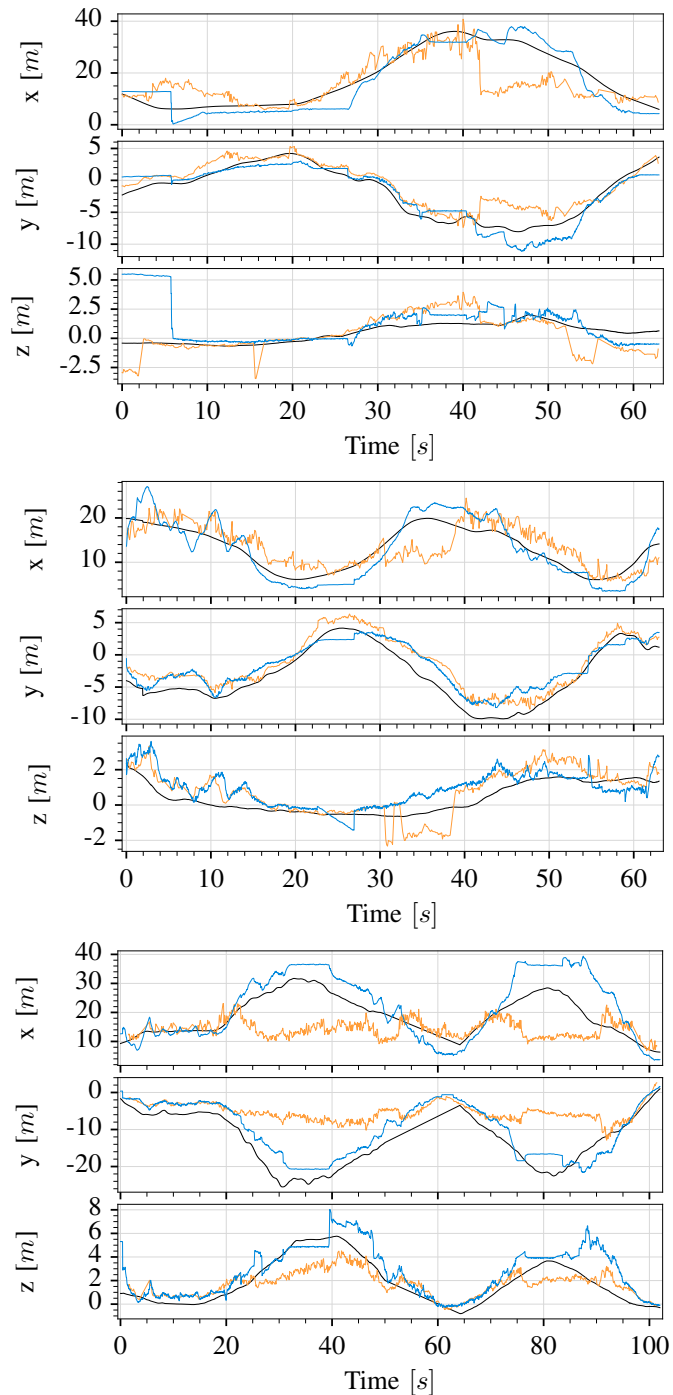


Fig. 10: Relative position estimates obtained using our approach (blue), *UVDAR* (orange), and the ground truth from RTK (black) for outdoor experiments 1–3 (from top to bottom).

V. CONCLUSION

This work presents a novel approach for onboard relative localization between tightly cooperating multi-robot teams. Our method estimates the relative position between UAVs by exploiting typically unwanted reflections of active localization markers attached to team members. By accounting for uncertainties introduced by camera resolution and surface irregularities, the proposed method operates without prior knowledge of team member sizes or surface properties. This makes it particularly well-suited for fast deployment on micro-UAVs flying in close formation in urban indoor and marine outdoor environments. We validated our approach in indoor experiments, demonstrating reliable performance without prior knowledge of team member sizes or surface properties, and robustness to varying lighting conditions. Outdoor experiments further showed that our method outperforms current state-of-the-art approaches, particularly at greater distances (> 30 m), reducing the MAE by up to 37.3% along the optical axis. These results demonstrate that our novel reflection-based approach provides a reliable and accurate solution for relative localization in challenging real-world environments.

ACKNOWLEDGEMENTS

This work was funded by CTU grant no SGS23/177/OHK3/3T/13, by the Czech Science Foundation (GAČR) under research project no. 23-07517S and by the European Union under the project Robotics and advanced industrial production (reg. no. CZ.02.01.01/00/22_008/0004590).

REFERENCES

- [1] T. H. Nguyen and L. Xie, "Relative transformation estimation based on fusion of odometry and uwb ranging data," *IEEE Transactions on Robotics*, vol. 39, no. 4, pp. 2861–2877, 2023.
- [2] Z. Zhang, H. Yuan, X. He, B. Li, and J. Geng, "Best Integer Equivariant Estimation With Quality Control in GNSS RTK for Canyon Environments," *IEEE Transactions on Aerospace and Electronic Systems*, vol. 59, no. 4, pp. 4105–4117, 2023-08.
- [3] Y. Gao, J. Yuan, J. Jiang, Q. Sun, and X. Zhang, "VIDO: A Robust and Consistent Monocular Visual-Inertial-Depth Odometry," *IEEE Transactions on Intelligent Transportation Systems*, vol. 24, no. 3, pp. 2976–2992, 2023-03.
- [4] T.-M. Nguyen, Z. Qiu, T. H. Nguyen, M. Cao, and L. Xie, "Distance-Based Cooperative Relative Localization for Leader-Following Control of MAVs," *IEEE Robotics and Automation Letters*, vol. 4, no. 4, pp. 3641–3648, 2019-10.
- [5] H. Stuckey, A. Al-Radaideh, L. Escamilla, L. Sun, L. G. Carrillo, and W. Tang, "An optical spatial localization system for tracking unmanned aerial vehicles using a single dynamic vision sensor," in *2021 IEEE/RSJ International Conference on Intelligent Robots and Systems (IROS)*, 2021, pp. 3093–3100.
- [6] S. Scheideman, N. Ray, and H. Zhang, "A flexible method for performance evaluation of robot localization," in *2020 IEEE International Conference on Robotics and Automation (ICRA)*, 2020, pp. 8302–8308.
- [7] H. Xu, L. Wang, Y. Zhang, K. Qiu, and S. Shen, "Decentralized Visual-Inertial-UWB Fusion for Relative State Estimation of Aerial Swarm," in *2020 IEEE International Conference on Robotics and Automation (ICRA)*, 2020-05, pp. 8776–8782.
- [8] F. Schilling, F. Schiano, and D. Floreano, "Vision-Based Drone Flocking in Outdoor Environments," *IEEE Robotics and Automation Letters*, vol. 6, no. 2, pp. 2954–2961, 2021-04.
- [9] L. Teixeira, F. Maffra, M. Moos, and M. Chli, "VI-RPE: Visual-Inertial Relative Pose Estimation for Aerial Vehicles," *IEEE Robotics and Automation Letters*, vol. 3, no. 4, pp. 2770–2777, 2018-10.
- [10] E. Olson, "Apriltag: A robust and flexible visual fiducial system," in *2011 IEEE International Conference on Robotics and Automation*, 2011, pp. 3400–3407.
- [11] H. Stuckey, L. Escamilla, L. R. Garcia Carrillo, and W. Tang, "Real-Time Optical Localization and Tracking of UAV Using Ellipse Detection," *IEEE Embedded Systems Letters*, vol. 16, no. 1, pp. 1–4, 2024-03.
- [12] V. Walter, N. Staub, A. Franchi, and M. Saska, "UVDAR System for Visual Relative Localization With Application to Leader-Follower Formations of Multirotor UAVs," *IEEE Robotics and Automation Letters*, vol. 4, no. 3, pp. 2637–2644, 2019-07.
- [13] M. Faessler, E. Mueggler, K. Schwabe, and D. Scaramuzza, "A monocular pose estimation system based on infrared leds," in *2014 IEEE International Conference on Robotics and Automation (ICRA)*, 2014, pp. 907–913.
- [14] K. Berger, R. Voorhies, and L. H. Matthies, "Depth from stereo polarization in specular scenes for urban robotics," in *2017 IEEE International Conference on Robotics and Automation (ICRA)*, May 2017, pp. 1966–1973.
- [15] Y. Li, S. Lin, H. Lu, S. B. Kang, and H.-Y. Shum, "Multibaseline stereo in the presence of specular reflections," in *2002 International Conference on Pattern Recognition*, vol. 3, 2002, pp. 573–576.
- [16] X. Huang, C. Wu, X. Xu, B. Wang, S. Zhang, C. Shen, C. Yu, J. Wang, N. Chi, S. Yu, and C. Chang-Hasnain, "Polarization structured light 3d depth image sensor for scenes with reflective surfaces," *Nature Communications*, vol. 14, 10 2023.
- [17] Z. Li, P. Wang, K. Liu, and Z. Tian, "MimoLoc: Indoor Localization With Assistance of Microwave Reflection of Downlink Signal in Sub-6G MIMO Networks," *IEEE Transactions on Microwave Theory and Techniques*, vol. 72, no. 4, pp. 2655–2668, Apr. 2024.
- [18] Z. Li, P. Wang, Z. Tian, and K. Liu, "TriLoc: Toward Accurate Indoor Localization With Assistance of Microwave Reflections," *IEEE Transactions on Microwave Theory and Techniques*, vol. 71, no. 6, pp. 2734–2747, Jun. 2023.
- [19] G. Zhang, D. Zhang, Y. He, J. Chen, F. Zhou, and Y. Chen, "Multi-Person Passive WiFi Indoor Localization With Intelligent Reflecting Surface," *IEEE Transactions on Wireless Communications*, vol. 22, no. 10, pp. 6534–6546, Oct. 2023.
- [20] I. An, Y. Kwon, and S.-e. Yoon, "Diffraction- and Reflection-Aware Multiple Sound Source Localization," *IEEE Transactions on Robotics*, vol. 38, no. 3, pp. 1925–1944, Jun. 2022.
- [21] L. I. Birnie, T. D. Abhayapala, and P. N. Samarasinghe, "Reflection Assisted Sound Source Localization Through a Harmonic Domain MUSIC Framework," *IEEE/ACM Transactions on Audio, Speech, and Language Processing*, vol. 28, pp. 279–293, 2020.
- [22] L. Yang, J. Liu, and X. Tang, "Depth from water reflection," *IEEE Transactions on Image Processing*, vol. 24, no. 4, pp. 1235–1243, 2015.
- [23] D. Bonilla Licea, V. Walter, M. Ghogho, and M. Saska, "Optical communication-based identification for multi-uav systems: theory and practice," *Autonomous Robots*, vol. 49, no. 3, p. 24, Sep 2025.
- [24] M. Born, E. Wolf, A. B. Bhatia, P. C. Clemmow, D. Gabor, A. R. Stokes, A. M. Taylor, P. A. Wayman, and W. L. Wilcock, *Principles of Optics: Electromagnetic Theory of Propagation, Interference and Diffraction of Light*, 7th ed. Cambridge University Press, 1999.
- [25] E. Hecht, *Optics*, ser. Pearson education. Addison-Wesley, 2002.
- [26] T. Thomas, "Characterization of surface roughness," *Precision Engineering*, vol. 3, no. 2, pp. 97–104, 1981.
- [27] M. Berhanu, E. Falcon, and L. Deike, "Turbulence of capillary waves forced by steep gravity waves," *Journal of Fluid Mechanics*, vol. 850, p. 803–843, 2018.
- [28] D. Scaramuzza, A. Martinelli, and R. Siegwart, "A Flexible Technique for Accurate Omnidirectional Camera Calibration and Structure from Motion," in *Fourth IEEE International Conference on Computer Vision Systems (ICVS'06)*, 2006-01, pp. 45–45.
- [29] D. Hert, T. Baca, P. Petracek *et al.*, "MRS Drone: A Modular Platform for Real-World Deployment of Aerial Multi-Robot Systems," *Journal of Intelligent & Robotic Systems*, vol. 108, no. 4, p. 64, Aug. 2023.
- [30] J. Horyna, V. Krátký, V. Pritzl, T. Báča, E. Ferrante, and M. Saska, "Fast Swarming of UAVs in GNSS-Denied Feature-Poor Environments Without Explicit Communication," *IEEE Robot. Autom. Lett.*, vol. 9, no. 6, pp. 5284–5291, Jun. 2024.